Phys. Status Solidi A **206**, No. 7, 1631–1635 (2009) / **DOI** 10.1002/pssa.200824458

physica status solidi a
www.pss-a.com
applications and materials science

Low thermal resistance, high-speed 980 nm asymmetric intracavity-contacted oxide-aperture VCSELs

Y. M. Song[1], K. S. Chang[2], B. H. Na[1], J. S. Yu[3], and Y. T. Lee[*, 1]

[1] Department of Information and Communications, Gwangju Institute of Science and Technology, 1 Oryong-dong, Buk-gu, Gwangju 500-712, Korea
[2] Division of Instrument Development, Korea Basic Science Institute, 113 Gwahangno, Yusung-gu, Daejeon 305-333, Korea
[3] Department of Electronic Engineering, Kyung Hee University, 1, Seocheon-dong, Giheung-gu, Yongin-si, Gyeonggi-do 446-701, Korea

Received 6 November 2008, revised 12 February 2009, accepted 12 February 2009
Published online 22 April 2009

PACS 42.55.Px, 81.05.Ea, 85.35.Be, 85.60.Bt

[*] Corresponding author: e-mail ytlee@gist.ac.kr

We demonstrated high-speed characteristics of an oxide-aperture vertical-cavity surface-emitting laser (VCSEL) with intracavity structures for both p- and n-contacts, based on InGaAs/GaAs multiple quantum wells operating at $\lambda \sim 980$ nm, indicating a low thermal resistance (R_{th}). The asymmetric current injection scheme is employed for reducing current crowding around the rim of the oxide aperture. A high aluminium content undoped $Al_{0.88}Ga_{0.12}As$ and GaAs distributed Bragg reflector (DBR) mirror is used for efficient heat dissipation. The VCSEL with a 7 µm oxide aperture exhibited an output power of 2.5 mW and a threshold current of 0.8 mA with a slope efficiency of 0.39 mW/mA at 20 °C under continuous-wave operation and it still worked with 1.3 mW at 90 °C. The temperature tuning coefficient of 0.081 nm/°C and dissipated electrical power tuning coefficient of 0.104 nm/mW were observed, leading to a low R_{th} of 1.28 °C/mW. A high modulation bandwidth up to 13 GHz with a modulation current efficiency factor of 6.1 GHz/mA$^{1/2}$ was achieved.

© 2009 WILEY-VCH Verlag GmbH & Co. KGaA, Weinheim

1 Introduction Vertical-cavity surface-emitting lasers (VCSELs) have attracted great attention as a promising light source for high bit rate transmission and its application, especially above 10 Gbps, due to the low cost, small size, low power consumption, and high modulation bandwidth. The high-speed operation can be achieved by improving differential gain and by reducing the parasitic elements such as series resistance and pad capacitance. Also, the thermal characteristics play an importance role in the device performance. Intracavity-contacted VCSELs, formed by the undoped distributed Bragg reflector (DBR) mirrors and two contact layers on either side of the active region, are suitable to meet the requirements because of their many advantages such as low optical losses in both undoped DBRs, no complex composition/doping grading, and coplanar contacts resulting in reduced pad capacitance [1, 2]. Furthermore, the incorporation of additional process technologies into the DBR, such as photonic crystal [3], monolithic integration of microlens [4], and high-index contrast grating [5], is favorable in intracavity-contacted VCSEL structures because there is no current path across undoped DBR regions.

Recently, the VCSELs with the intracavity for only the lower contact (i.e., n contact) was demonstrated with a high speed of >20 GHz [6, 7], indicating a coplanar contact. But it is difficult to apply the additional processes to the p-doped top DBR. For VCSELs with undoped DBRs, where intracavity structures are applied at both p- and n-contacts on the bottom of mesas, the 3 dB modulation bandwidths up to 11 GHz have been reported [2, 8]. However, the current aperture of these devices was formed by a shallow implant which somewhat complicates the fabrication process because the mask should be relatively thick to block the high energy protons. The dielectric DBR mirrors

WILEY InterScience® DISCOVER SOMETHING GREAT

© 2009 WILEY-VCH Verlag GmbH & Co. KGaA, Weinheim

have poor thermal conductivity, causing an increase of the thermal resistance of the device. Therefore, the semiconductor DBRs with a high thermal conductivity are desirable. Additionally, the use of asymmetric current injection scheme results in a reduction of the current crowding effect [2]. In this paper, we report high-speed modulation of $\lambda \sim 980$ nm asymmetric intracavity-contacted (for both p- and n-contacts) oxide-aperture VCSELs with undoped $GaAs/Al_{0.88}Ga_{0.12}As$ DBRs, showing a maximum 3 dB modulation bandwidth of 13.1 GHz at a bias current of 10 mA. The thermal resistance is obtained from the output wavelength spectrum with respect to the temperature and dissipated electrical power changes. The parasitic elements were also extracted from the equivalent circuit model.

2 Experiments The schematic illustration of the asymmetric intracavity-contacted oxide-aperture VCSELs with a corresponding equivalent circuit model is shown in Fig. 1. All epitaxial layers were grown on semi-insulating GaAs substrate by using a molecular beam epitaxy (DCA P600). The intracavity structures were formed for both n- and p-contacts. The top and bottom DBR mirrors consists of 22 and 30.5 pairs of undoped $GaAs/Al_{0.88}Ga_{0.12}As$ layers, respectively. The active region consists of 1 λ cavity with three $In_{0.19}Ga_{0.81}As/GaAs$ (8.5 nm/10 nm) quantum wells surrounded by $Al_{0.3}Ga_{0.7}As$ cladding layers. The cavity is bounded on each side by $Al_{0.98}Ga_{0.02}As$ oxidation layers, followed by p- and n-doped GaAs contact layers. The thickness of contact layers was optimized at 5/4 λ in order to suppress the current crowding effects and to reduce the series resistance [9].

For device fabrication, the wafer was processed into the first cylindrical mesas of 18 μm in diameter etched down to the p-GaAs contact layer in $SiCl_4/Ar$ (7.5 sccm/25 sccm) plasma by using an inductively coupled plasma etcher. Then, the second cylindrical mesas of 54 μm in diameter were etched down to the n-GaAs contact layer. Two $Al_{0.98}Ga_{0.02}As$ layers were selectively oxidized by a wet thermal oxidation process for electrical and optical confinement, keeping the oxide aperture diameter of 7 μm. The n-contact layer was etched for device isolation and benzocyclobutene (BCB) was coated on the sample and cured at 210 °C for 1 h for passivation and planarization. After exposing the p- and n-GaAs contact layers in CF_4/O_2 (45 sccm/5 sccm) plasma by using a reactive ion etcher, Pt/Ti/Pt/Au (10 nm/10 nm/40 nm/500 nm) and Ni/Au/Ge/Ni/Au (20 nm/100 nm/50 nm/30 nm/500 nm) metals were deposited on the p- and n-GaAs contact layers by using an e-beam evaporator, respectively. To reduce the current crowding at the perimeter of the oxide aperture the p- and n-contacts were formed asymmetrically to the opposite side with an alloying cycle at 425 °C for 25 s. The fabricated devices were bonded on a copper heatsink using indium solder, and loaded onto the thermoelectric cooler mount. The thermistor is located within the mount to control the temperature of the device. The testing was performed over the temperature range of 20–90 °C under continuous-wave (CW) mode.

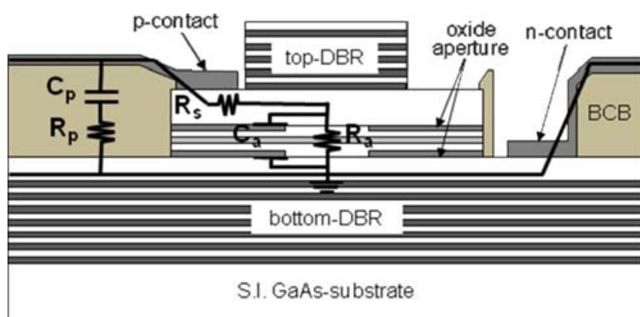

Figure 1 (online colour at: www.pss-a.com) Schematic illustration of the asymmetric intracavity-contacted oxide-aperture VCSELs with a corresponding equivalent circuit model.

3 Results and discussion Figure 2 shows the light–current ($L-I$) curves over the temperature range of 20–90 °C (steps of 10 °C) under CW mode for the VCSELs with a 7 μm oxide aperture. The current–voltage ($I-V$) curves at 20 °C and 90 °C are also shown. The scanning electron microscope (SEM) image of a fabricated device is also displayed in the inset of Fig. 2. The device exhibits a threshold current of $I_{th} = 0.8$ mA and a slope efficiency ($\eta = dP/dI$, where P is the output power and I is the injection current) of 0.39 mW/mA at 20 °C. The differential series resistance is approximately 180 Ω, maybe resulting from the insufficient doping of the contact layers and the long lateral conduction length. The maximum output power of 2.52 mW at 20 °C was obtained around 12 mA and it still operated with an output power of 1.3 mW at 90 °C. It is noted that the maximum output power decreases with increasing the temperature due to the spectral misalignment by temperature-induced heating effects. The threshold voltage is kept almost constant with the range of 2.20–2.29 V between 20 °C and 90 °C.

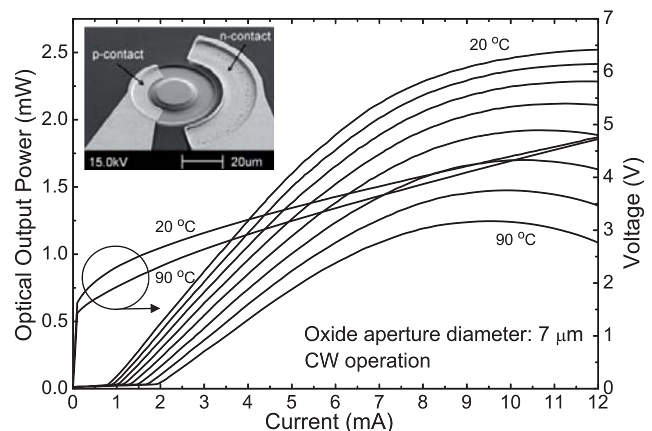

Figure 2 $L-I$ curves over the temperature range of 20–90 °C (steps of 10 °C) under CW mode for the VCSELs with a 7 μm oxide aperture. $I-V$ curves at 20 °C and 90 °C are also shown. The inset shows the SEM image of a fabricated device.

© 2009 WILEY-VCH Verlag GmbH & Co. KGaA, Weinheim

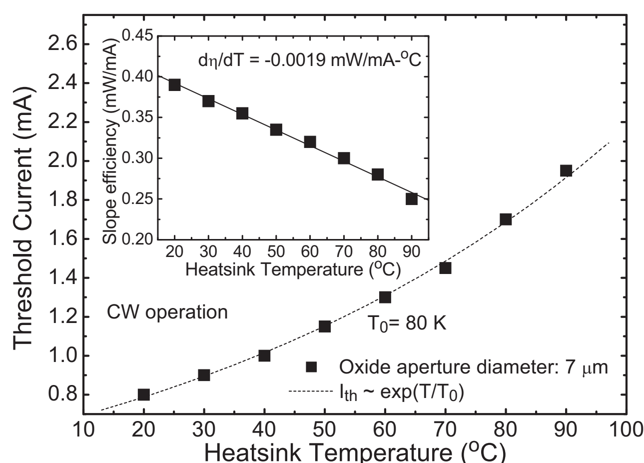

Figure 3 Threshold current as a function of heatsink temperature in CW operation for the VCSELs with a 7 μm oxide aperture. The inset shows the slope efficiency as a function of heatsink temperature.

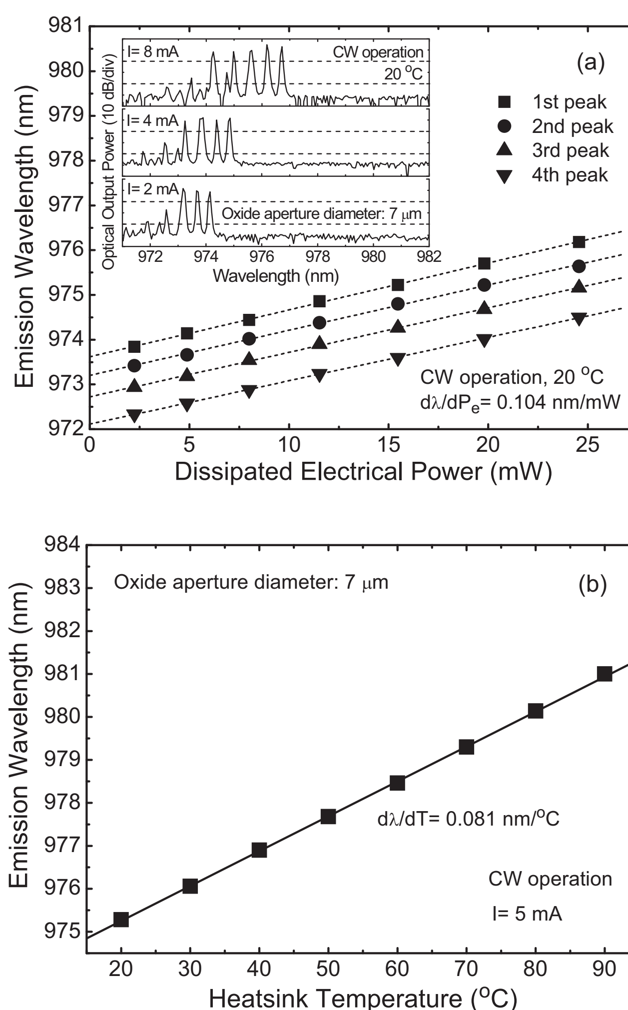

Figure 4 (a) Emission wavelength as a function of dissipated electrical power for 1st, 2nd, 3rd, and 4th peaks obtained from the emission spectra, and (b) emission wavelength as a function of heatsink temperature measured at a constant injection current of $I = 5$ mA. The inset of (a) shows the CW emission spectra of the VCSELs with a 7 μm aperture diameter under injection currents of 2 mA, 4 mA, and 8 mA at 20 °C.

As the temperature is increased from 20 °C to 90 °C, the threshold current is increased from 0.8 mA to 1.95 mA due to the reduction of peak gain and the increase of leakage. The threshold current as a function of heatsink temperature in CW operation for the VCSELs with a 7 μm oxide aperture is plotted in Fig. 3. The temperature dependence of threshold current can be well described phenomenologically by a usual exponential function of $I_{th} \sim \exp(T/T_0)$, where T is the heatsink temperature and T_0 is the characteristic temperature. From the curve fitting using the above equation, the characteristic temperature of 80 K was obtained. As shown in the inset of Fig. 3, the slope efficiency of the device is decreased from $\eta = 0.39$ mW/mA at 20 °C to $\eta = 0.25$ mW/mA at 90 °C with the increase of heatsink temperature, indicating $d\eta/dT = -0.0019$ mW/mA °C. The η values translate into differential quantum efficiency (η_d) values of 31% and 20% at 20 °C and 90 °C, respectively. Here, $\eta_d = (e/h\nu)(dP/dI)$, where e is the electron charge and $h\nu$ is the photon energy.

In order to estimate the thermal resistance of the fabricated VCSEL, the output wavelength spectra with respect to the temperature and dissipated electrical power changes were measured. For spectrum measurements, the output light is coupled into an optical spectrum analyzer using a single multimode fiber. Figure 4(a) shows the emission wavelength as a function of dissipated electrical power for 1st, 2nd, 3rd, and 4th peaks obtained from the emission spectra. The dissipated electrical power is defined as the input electrical power minus the output optical power. The inset of Fig. 4(a) shows the CW emission spectra of the VCSELs with a 7 μm aperture diameter under injection currents of 2 mA, 4 mA, and 8 mA at 20 °C. The measured spectrum exhibited typical multimode characteristics with emission peaks around 975 nm. Peak wavelengths are red-shifted toward longer wavelengths as the dissipated electrical power is increased. The wavelength of the 1st peak was changed from 973.9 mW at 2.3 mW to 976.2 nm at 24.5 mW, corresponding to a dissipated electrical power tuning coefficient ($d\lambda/dP_e$) of ~0.104 nm/mW. The others also give similar values, leading to the linear tuning characteristics of the wavelength with dissipated electrical power. The emission wavelength as a function of heatsink temperature measured at a constant injection current of $I = 5$ mA is shown in Fig. 4(b). From the straight line fitting, the wavelength of the first peak is increased from 975.3 nm at 20 °C to 981 nm at 90 °C, which gives a temperature tuning coefficient of 0.081 nm/°C. The thermal resistance can be determined by a simple relationship of $R_{th} = \Delta T/\Delta P_e = (\Delta\lambda/\Delta P_e)/(\Delta\lambda/\Delta T)$ [10]. The corresponding thermal resistance of $R_{th} = 1.28$ °C/mW was obtained.

© 2009 WILEY-VCH Verlag GmbH & Co. KGaA, Weinheim

This value is lower than that of intracavity-contacted VCSELs with dielectric DBRs reported previously (i.e., 1.95 °C/mW) [11] and is also similar to that of extracavity contacted VCSELs with a thick electroplated copper for efficient heat dissipation [12]. In intracavity-contacted VCSEL structure, the heat generation inside device is presumably less because there is no heat source in thick DBR layers compared to extracavity contacted structure. Moreover, the use of high aluminium content $Al_{0.88}Ga_{0.12}As$ (i.e., thermal conductivity of $\kappa = 22.69$ W/m K) and GaAs (i.e., $\kappa = 44$ W/m K) DBR pairs with a higher thermal conductivity than dielectric DBRs should help to dissipate more easily the heat generated from the active region, thus resulting in the lower thermal resistance.

The small-signal modulation response was measured using a 30 GHz RF spectrum analyzer with 25 GHz high-speed photodetector. 40 GHz bias tee was used to combine DC bias and RF signal from 20 GHz CW generator. Figure 5 shows a small signal modulation response of the VCSEL with a 7 μm oxide aperture at different bias currents at 20 °C. The modulation response can be fitted by [13]

$$|M(f)|^2 = \left(\frac{f_r^4}{\left(f_r^2 - f^2\right)^2 + (\gamma/2\pi)^2 f^2} \right) \cdot |P(f)|^2 , \qquad (1)$$

where f_r is the resonance frequency, γ is the damping rate, and $P(f)$ is the parasitic circuit effect. From the measured data and curve fitting, a maximum 3 dB modulation bandwidth of 13.1 GHz was obtained at a bias current of 10 mA. The modulation current efficiency factor (MCEF), i.e., a linear interrelationship between the 3 dB modulation bandwidth and the square root of the driving current above threshold, was approximately 6.1 GHz/mA$^{1/2}$ as shown in the inset of Fig. 5.

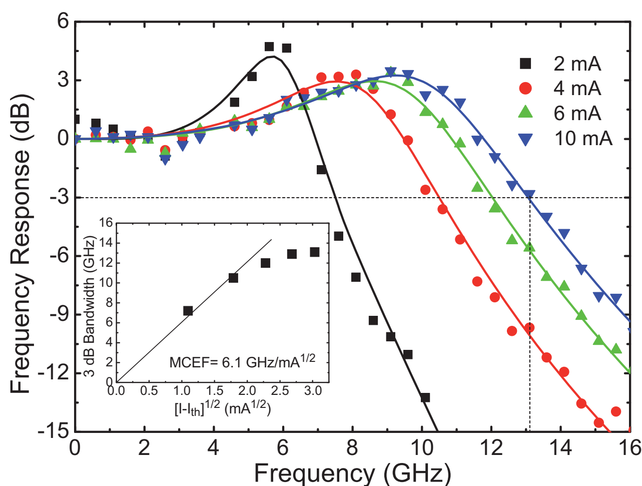

Figure 5 (online colour at: www.pss-a.com) Small signal modulation response of the VCSEL with a 7 μm oxide aperture at different bias currents at 20 °C. The solid lines are fittings to the three pole filter function. The inset shows the modulation current efficiency factor of VCSELs.

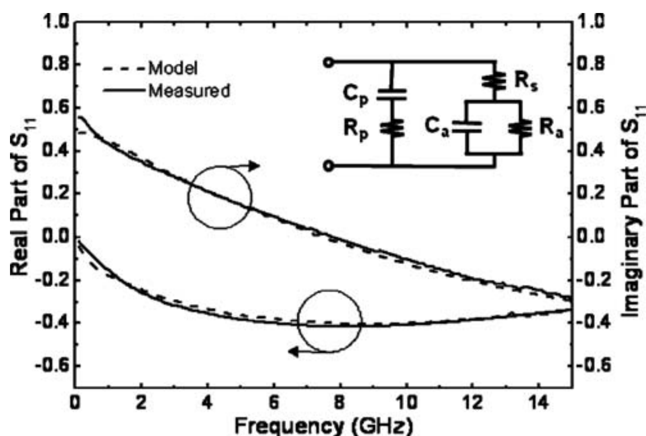

Figure 6 Measured and fitted S_{11} results for asymmetric intracavity-contacted oxide-aperture VCSELs with a 7 μm oxide aperture. The inset shows the equivalent circuit model of asymmetric intracavity-contacted oxide aperture VCSELs.

To analyze parasitic elements of the asymmetric intracavity-contacted oxide-aperture VCSELs, the equivalent circuit model was used as shown in Fig. 1. The C_p and R_p are the pad capacitance and shunt resistance, respectively. The R_a represents the resistance in active region and the C_a contains capacitance of the active area and oxide layer. The R_s corresponds to the series resistance, which occurs not in the DBR mirrors but in the lateral conduction region. The parameters were extracted by the fits of the measured S_{11} data from 100 MHz to 15 GHz. Figure 6 shows the measured and fitted S_{11} results for asymmetric intracavity-contacted oxide-aperture VCSELs with a 7 μm oxide aperture. The extracted values of C_p, R_p and R_s were 260 fF, 21 Ω and 86 Ω, respectively, and the resulting R_a and C_a values, which vary with bias current, were 23 Ω and 1.5 pF at the bias current of 10 mA. The value of R_s is not small enough compared to the mirror resistance R_m value of extracavity-contacted VCSELs [14], mainly because the lateral conduction length is long. The pad capacitance C_p is smaller than extracavity-contacted VCSEL structures due to coplanar contacts, whereas the C_a value is very large due to the relatively large area of oxide layer. Therefore, with a further reduction in the series resistance (R_s) and active capacitance (C_a) by optimizing the first/second mesa diameters and the doping, the device performance is expected to be improved.

4 Conclusions

We have demonstrated the high-speed operation of oxide-aperture VCSELs with asymmetric intracavity structures for both p- and n-contacts and with undoped DBR mirrors operating at $\lambda \sim 980$ nm. For the VCSEL with a 7 μm oxide aperture, a maximum output power of 2.52 mW and a slope efficiency of 0.39 mW/mA at 20 °C were obtained and it operated above 90 °C

© 2009 WILEY-VCH Verlag GmbH & Co. KGaA, Weinheim

with a characteristic temperature of $T_0 = 80$ K. The device exhibited a low thermal resistance of 1.28 °C/mW, which was extracted from the emission wavelength changes with respect to the temperature and dissipated electrical power changes, i.e., $d\lambda/dT = 0.081$ nm/°C and $d\lambda/dP_e = 0.104$ nm/W. A high modulation bandwidth up to 13.1 GHz was achieved with an MCEF of 6.1 GHz/mA$^{1/2}$, making these devices suitable for high-speed transmission applications.

Acknowledgement This work was supported by GIST Top Brand Project "Photonics 2020".

References

[1] J. W. Scott, B. J. Thibeault, D. B. Young, L. A. Coldren, and F. H. Peters, IEEE Photon. Technol. Lett. **6**, 678 (1994).
[2] A. V. Krishnamoorthy, L. M. F. Chirovsky, W. S. Hobson, J. Lopata, J. Shah, R. Rozier, J. E. Cunningham, and L. A. D'Asaro, IEEE Photon. Technol. Lett. **12**, 609 (2000).
[3] P. O. Leisher, A. J. Danner, and K. D. Choquette, IEEE Photon. Technol. Lett. **18**, 2156 (2006).
[4] K. S. Chang, Y. M. Song, and Y. T. Lee, IEEE Photon. Technol. Lett. **18**, 2203 (2006).
[5] I. S. Chung, J. Mork, P. Gilet, and A. Chelnokov, IEEE Photon. Technol. Lett. **20**, 105 (2008).
[6] N. Suzuki, H. Hatakeyama, K. Tokutome, K. Fukatsu, M. Yamada, T. Anan, and M. Tsuji, IEEE Photon. Technol. Lett. **18**, 1368 (2006).
[7] Y. C. Chang, C. S. Wang, and L. A. Coleren, Electron. Lett. **43**, 1022 (2007).
[8] G. Dang, W. S. Hobson, L. M. F. Chirovsky, J. Lopata, M. Tayahi, S. N. G. Chu, F. Ren, and S. J. Pearton, IEEE Photon. Technol. Lett. **13**, 924 (2001).
[9] V. V. Lysak and Y. T. Lee, J. Optoelectron. Adv. Mater. **8**, 1601 (2006).
[10] T. Wipiejewski, D. B. Young, M. G. Peters, B. J. Thibeault, and L. A. Coldren, Electron. Lett. **31**, 279 (1995).
[11] A. N. Al-Omari, G. P. Carey, S. Hallstein, J. P. Watson, G. Dang, and K. L. Lear, IEEE Photon. Technol. Lett. **18**, 1225 (2006).
[12] G. Dang, B. Luo, F. Ren, W. S. Hobson, J. Lopata, S. J. Pearton, W. Chang, and H. Shen, Solid-State Electron. **46**, 1247 (2002).
[13] R. Nagarajan, T. Fukushima, J. E. Bowers, R. S. Geels, and L. A. Coldren, Appl. Phys. Lett. **58**, 2326 (2001).
[14] Y. H. Chang, H. C. Kuo, F. I. Lai, K. F. Tzeng, H. C. Yu, C. P. Sung, H. P. Yang, and S. C. Wang, IEE Proc. Optoelectron. **152**, 170 (2005).

© 2009 WILEY-VCH Verlag GmbH & Co. KGaA, Weinheim